Letters

Spectrum Estimation of Input Current Ripple on a Wide Class of Multilevel Grid-Tied Converters

Davide Biadene, *Member, IEEE*

Abstract—**Multilevel (ML) converters are frequently used to implement grid-tied ac–dc conversion systems. Their design may benefit from multiobjective optimization techniques, which typically involves time-consuming circuit simulations in order to obtain input current estimations suitable for input inductor and electromagnetic interference filter design. Herein, a closed-form expression of the input current ripple is derived to ease harmonic content estimations. The proposed approach separates the fundamental grid-current component from its ripple and models the latter like an amplitude modulation, where the modulating signal is its envelope and the carrier is the triangular current waveform. First, a general waveform analysis of ML converters is performed to derive the voltage across the grid-side inductor, then the associated current ripple is modeled. Experimental results on an ML converter prototype are reported to validate the analytical results.**

Index Terms—**AC–DC converter, electromagnetic interference (EMI) filter, input filter design, multiobjective optimization, multilevel (ML) converters, pulsewidth modulation (PWM) rectifier.**

I. INTRODUCTION

IN INDUSTRIAL applications, the energy supply chain may involve high-power ac–dc converter systems interlinking medium/high-voltage (MV/HV) ac transmission lines and in-house ac or dc loads connected by means of a second conversion stage. Multilevel (ML) converter topologies are widely used at the ac-grid side by virtue of their features: First, they are often implemented with input-series connected modules sharing the MV/HV voltage and, hence, the input power, allowing a significant increase in efficiency respect other solutions (e.g., two-level inverter); second, they provide high performance in terms of harmonic distortion and EMI compliance mostly related to conducted emissions [1], [2].

A typical application is on power factor correction (PFC) systems, where the aim is to increase the power factor by exchanging sinusoidal currents that are in-phase with the grid voltage in order to minimize the reactive power circulating through the
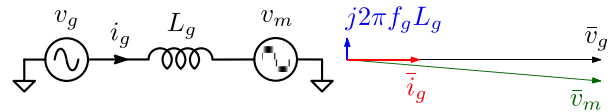
Fig. 1. Simplified PFC application of MV-converter and phasor representation.

distribution grid. As shown in Fig. 1, the converter control shapes the input voltage $v_m(t)$ through the filter inductance L_g to absorb the desired input current $\bar{i}_g$ in-phase with the input grid voltage $\bar{v}_g$

$$\bar{v}_m = \bar{v}_g - j2\pi f_g L_g \bar{i}_g \tag{1}$$

where $\bar{v}_g$ and $\bar{v}_m$ are the phasor representations of the grid voltage $v_g(t)$ and the fundamental component of the ML-converter voltage $v_m(t)$, respectively, defined as $v_x(t) = \Re\{\bar{v}_x e^{j2\pi f_g t}\}$ with f_g the grid frequency. To generate (1), ML converters exploit an N_L-level voltage waveform. In the following analysis, a particular class of ML converters is considered where the voltage levels are equally spaced by a quantity V_N, and the generated voltage can switch only between two consecutive levels in a switching period T_m of the converter. An example of the generated voltage by an 11-level converter and the absorbed current from the grid in a positive half-wave are displayed in Fig. 2(a) and (b). The average values $\langle\cdot\rangle_{T_m}$ computed within a switching period T_m are also indicated, where $\langle\cdot\rangle_T$ denotes the moving average operator, that is, $\langle\cdot\rangle_T = 1/T \int_{t-T}^{t} \cdot\, d\tau$. Fig. 2(c) shows the generic waveforms v_m and i_g within of two consecutive switching periods T_m.

In the design process, especially when multiobjective optimization approaches are used, the knowledge of the harmonic content of grid current i_g is crucial for the design of filter inductor L_g and input EMI filter. The power losses of the filter components can be easily calculated by the superposition of losses related to each frequency of the current spectrum (e.g., winding and core losses in the inductors).

In the literature, the grid current spectrum is often obtained by computer simulation, which is typically very time-consuming. In fact, the minimum spectrum resolution should equal f_g in order to correctly appreciate the sideband harmonics; then, the simulation time should cover at least 20 ms of steady-state operation while to reach the frequency range of conducted emissions (i.e., 9 kHz–30 MHz) the maximum simulation time-step
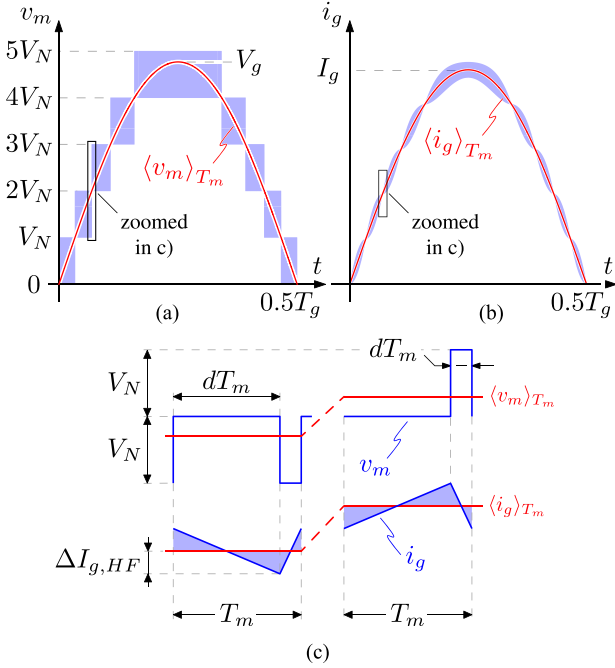
Fig. 2. Main waveforms of ML converter at positive half-wave. (a) Input voltage. (b) Input current. (c) Zoom-in of input voltage and input current in switching period highlighting the differences of waveforms between two consecutive couples of voltage levels.

Fig. 3. Graphs of the functions $(\cdot)_K$ and $(\cdot)_f$ for different values of N_L. (a) N_L odd. (b) N_L even. Domain and codomain of the functions depending on the number of levels N_L are highlighted, the inner areas are related to N_L equal to 3 and 2.

should be lower than 16.7 ns (i.e., 1/60 MSps) [3], [4], [5]. On this basis, each design of a multiobjective optimization would collect $\geq$ 1.2 G samples of the input current to ensure compliance with conducted emissions standards. Alternatively, double Fourier integral analysis [6] on the grid current i_g is possible too, but this approach is always solved numerically and requires a high computation cost when the number of voltage levels increases [7], [8].

In the following, a spectrum model to estimate the input current ripple on the considered class of ML converters is proposed. The rest of this letter is organized as follows. Specifically, Section II provides the theoretical basis of the presented model. Section III demonstrates the model considering experimental results from an ML-converter prototype. Finally, Section IV concludes this letter.

II. SPECTRUM MODEL OF ML CURRENT RIPPLE

Two main assumptions have been done in the considered class of ML converters: 1) The voltage waveform v_m produced by the ML converter can be associated with a staircase waveform whose step amplitude is constant and constrained to switch between two consecutive voltage levels of the allowed N_L for each switching period T_m (e.g., V_N and $2V_N$, $2V_N$ and $3V_N$, etc.); 2) the voltage pulse changes position when ML-converter average voltage moves through next couple of consecutive voltage levels such that the current ripple waveform is mirrored around its average value $\langle i_g \rangle_{T_m}$, as shown in Fig. 2(c). These assumptions are valid for example in interleaved-PWM ML converters [9].
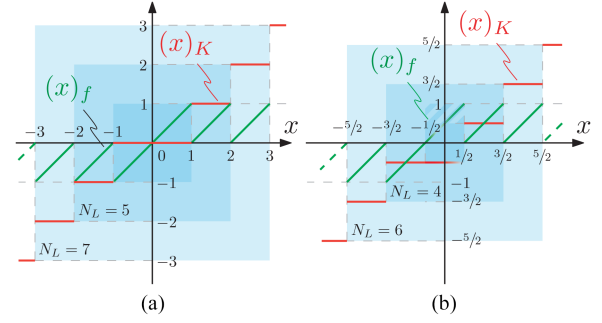
This approach is independent of the selected modulation scheme and topology of the ML converter: The number of modules can determine both the possible voltage levels N_L, and the switching period T_m using interleaving PWM strategies to multiply the switching frequency of the single module.

Considering the general voltage waveform depicted in Fig. 2(c) in the switching period T_m, it is characterized by a voltage pulse of amplitude V_N and width dT_m that leans on an offset voltage $k_s V_N$. Since the voltage levels must be bipolar, k_s can assume different values depending on the total number of levels N_L allowed by the ML converter. For the converter class discussed herein, k_s is limited in the following set K, depending on the parity of N_L as

$$k_s = \begin{cases} s & N_L \text{ odd}, \ s \in \left[-\frac{N_L-1}{2}, \frac{N_L-1}{2}\right] \\ s - \frac{1}{2}\operatorname{sign}(s) & N_L \text{ even}, \ s \in \left[-\frac{N_L}{2}, \frac{N_L}{2}\right] \setminus \{0\} \end{cases} . \quad (2)$$

To establish the modulation parameters of the voltage waveform (i.e., the duty cycle d and the base level voltage $k_s V_N$), the functions $(\cdot)_S$ and $(\cdot)_f$ are now defined as

$$(x)_S = \underset{s \in S, |s| < |x|}{\operatorname{argmin}} |x - s|$$

$$(x)_f = x - (x)_S \quad (3)$$

where the operator $(x)_S$ maps the argument into the closest s value in the set S, which is lower in a module to x. For the sake of clarity, Fig. 3 shows how the two functions $(\cdot)_K$ and $(\cdot)_f$ map a real number and which are their domain and codomain depending on the number of levels N_L. From Fig. 2(c), the average voltage in the switching period T_m can be expressed as

$$\langle v_m \rangle_{T_m} = k_s V_N \pm dV_N \quad (4)$$

where the sign is concordant with the v_m one. Using (3) in (4), the time trend of k and d values during a grid voltage period can be calculated as

$$k(t) = \left(\frac{\langle v_m(t) \rangle_{T_m}}{V_N}\right)_K \qquad d(t) = \left|\frac{\langle v_m(t) \rangle_{T_m}}{V_N}\right|_f \quad (5)$$

permitting to solve the input current spectrum and a closed form for its estimation. The absolute notation on $d(t)$ function

allows us to relate its value to the meaning of duty-cycle of the voltage pulse depicted in Fig. 2(c). Defining the high-frequency (HF) current component $i_{g,\text{HF}}$ as the difference between the grid current i_g and the fundamental harmonic component, namely, $i_{g,\text{HF}} = i_g - \langle i_g \rangle_{T_m}$, the current ripple can be calculated from the voltage across the grid-tied filter inductor v_L. Assuming a quasi-stationary condition, that is, the converter dynamics are neglected, being the operating point changing very slowly with respect to the switching period, the inductor voltage is

$$v_L = v_g - v_m = v_g - \langle v_m \rangle_{T_m} - v_{m,\text{HF}} \qquad (6)$$

where $v_{m,\text{HF}} = v_m - \langle v_m \rangle_{T_m}$ is the HF switching component of $v_L(t)$. Remarkably, the average voltage of ML converter is related to the grid current i_g by (1) allowing the further step on (6)

$$v_L = \omega_g L_g I_g \sin(\omega_g t) - v_{m,\text{HF}}. \qquad (7)$$

Assuming negligible the sinusoidal term, namely $\omega_g L_g I_g \ll V_N$, the voltage across the filter inductor can be just approximated to HF switching component of $v_L(t)$ (i.e., $v_L \approx -v_{m,\text{HF}}$).

This assumption is satisfied commonly in industrial applications where used values of the filter inductor bring $\omega_g L_g I_g / V_g < 0.05 \ldots 0.15$ [1]. As an initial consideration, this relationship defines a maximum value of N_L for which the spectrum approximation can be adopted. Exploiting the volt–second balance on the inductor L_g under the hypothesis above, the current ripple amplitude $\Delta I_{g,\text{HF}}$ is

$$\Delta I_{g,\text{HF}}(t) = \frac{V_N}{2 f_m L_g} d(t) \left[1 - d(t)\right] \qquad (8)$$

as displayed in Fig. 2(c). The ML converter is modulated such that $\langle v_m(t) \rangle_{T_m} \approx v_g(t)$ due to the negligible voltage drop on the filter inductor. Then, the effective duty cycle d can be derived from the grid voltage as follows:

$$d(t) = \left| \frac{v_g(t)}{V_N} \right|_f = |U_g \sin(2\pi f_g t)|_f \qquad (9)$$

where $U_g = V_g/V_N$, which is the grid voltage amplitude V_g normalized with respect to the step voltage V_N.

Substituting (9) into (8), the spectrum of the ripple current $\Delta I_{g,\text{HF}}$ is given by $\Delta \mathcal{I}_{g,\text{HF}} = \mathcal{F}\{\Delta I_{g,\text{HF}}\}$, where $\mathcal{F}(\cdot)$ indicates the Fourier transform operator. The presence of $(\cdot)_f$ in (9) impedes a straightforward estimation of the inductor current ripple because it is a nonlinear function and cannot be computed in a closed form. At this point, double Fourier integral analysis is the only tool to cope with the spectrum of (8) requiring a significant computation effort. However, the term $d(1 - d)$ in (8) is a parabolic function that can be well approximated by a sinusoidal term

$$d(1 - d) \approx \frac{\sin(\pi d)}{4}. \qquad (10)$$

The two functions reported in (10) are plotted in Fig. 4 depending on d value together with their difference Δf. The graph shows up the curves are close and the mismatch can be considered negligible in the estimation of the current ripple envelope. The same similarity is also reflected on the Fourier series expansions
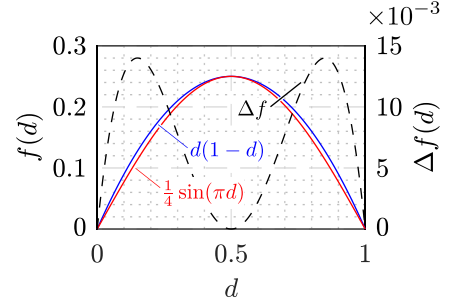

Fig. 4. Graphical representation of $\Delta I_{g,\text{HF}}$ term dependent on duty-cycle d with its sine approximation. The difference between the two curves Δf is drawn with a dashed line.
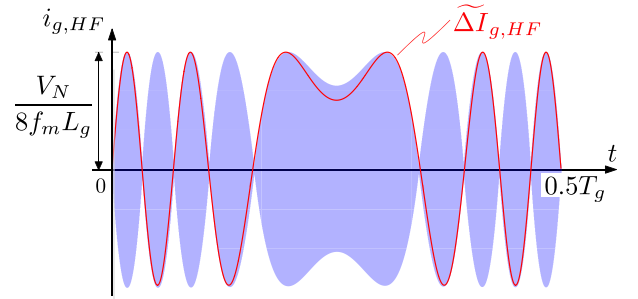

Fig. 5. Current ripple waveform $i_{g,\text{HF}}(t)$ and its estimated envelope $\widetilde{\Delta I}_{g,\text{HF}}(t)$ for the 11-levels ML converter in the positive grid half-wave.

of (10)

$$\frac{1}{6} - \sum_{n=1}^{+\infty} \frac{\cos(2n\pi d)}{2\pi^2 n^2} \approx \frac{1}{2\pi} - \sum_{n=1}^{+\infty} \frac{\cos(2n\pi d)}{2\pi(4n^2 - 1)}. \qquad (11)$$

In fact, looking at (11), the components of a parabolic term differ in module with respect to the sinusoidal one by 5% for the dc and the first-order harmonic components while by 15% to 20% for other components. This approximation leads the following estimate $\widetilde{\Delta I}_{g,\text{HF}}$ of the amplitude of the current ripple (8):

$$\widetilde{\Delta I}_{g,\text{HF}}(t) = \frac{V_N}{8 f_m L_g} \sin\left[\pi d(t)\right]. \qquad (12)$$

The next step should be the substitution of (9) into (12) but this brings a nonlinearity due to the function $(\cdot)_f$ again. However, exploiting the periodicity of sine in (10), the $(\cdot)_f$ operator can be removed because the sine function already maps periodically its argument to the interval $[-1, 1]$ taking into account also the phase change of the current ripple waveform between two consecutive levels. Moving from these premises, (12) becomes

$$\widetilde{\Delta I}_{g,\text{HF}}(t) = \frac{V_N}{8 f_m L_g} \Gamma(t)$$

$$\Gamma(t) = \begin{cases} \sin\left[\pi U_g \sin(2\pi f_g t)\right] & N_L \text{ odd} \\ \cos\left[\pi U_g \sin(2\pi f_g t)\right] & N_L \text{ even} \end{cases} \qquad (13)$$

where the nonlinear function $(\cdot)_f$ is substituted by the function Γ, which distinguishes the two cases related to the parity of N_L, since (2) implies a $1/2$ offset on d argument if N_L is even, as shown in Fig. 3(b). Fig. 5 reports both the HF current component

$i_{g,\mathrm{HF}}(t)$ and its estimated envelope $\widetilde{\Delta I}_{g,\mathrm{HF}}(t)$ for the 11-level converter in the positive grid half-wave of Fig. 2(a). Fig. 5 shows a close matching between (13) and the envelope of the HF current ripple of i_g.

Remarkably, (13) describes a phase-modulated (PM) signal, then, by the relevant modulation theory, the spectrum in terms of the Fourier series of the given signal can be found. The sine and cosine terms of (13) can be expanded using the Jacobi–Anger expansion [10], that is

$$e^{\pm iz\sin\theta} = J_0(z) + 2\sum_{n=1}^{+\infty} J_{2n}(z)\cos(2n\theta)$$
$$\pm 2i\sum_{n=0}^{+\infty} J_{2n+1}(z)\sin[(2n+1)\theta] \quad (14)$$

where $J_\nu(z)$ is a first-kind Bessel function.

Using (14) in (13), the resulting PM signal is composed of only the odd or even components around the fundamental harmonic (i.e., the grid component $\omega_g = 2\pi f_g$) accordingly to the N_L parity. The magnitude of the nth spectral component of the estimated current ripple amplitude $\widetilde{\Delta I}_{g,\mathrm{HF}}$ can be deduced by (13) as

$$\widetilde{\Delta\mathcal{I}}_{g,\mathrm{HF}}^n = \left|\mathcal{F}\left\{\widetilde{\Delta I}_{g,\mathrm{HF}}\right\}\right|_{f=nf_g} = \frac{V_N}{8f_mL_g}\left|J_n(\pi U_g)\right| \quad (15)$$

where n is odd or even based on the parity of N_L. Equation (13) describes the envelope of the HF current ripple as the modulating signal in an amplitude modulation where the carrier is the triangular wave of the inductor current. Since $i_{g,\mathrm{HF}}$ is a function of the duty-cycle d, also the harmonic components of its spectrum are affected by this dependence. Starting from Fig. 2(c), the HF current $i_{g,\mathrm{HF}}$ in a switching period T_m can be approximated to a scaled triangular wave as

$$y(\tau) = -y(-\tau) = \begin{cases} \frac{2\tau}{1-d}, & 0 \le \tau \le \frac{1-d}{2} \\ \frac{1-2\tau}{d}, & \frac{1-d}{2} \le \tau < \frac{1}{2} \end{cases} \quad (16)$$

where $\tau = t/T_m$ and d is specified by (9) at the considered instant. It is clear that (16) describes the current waveform in only a time frame of the grid period. Useful simplification can be also done to calculate the $i_{g,\mathrm{HF}}$ carrier spectrum looking to the Fourier series coefficients of (16) reported herein, rather than substitute d with (9) merely

$$|\mathcal{F}\{y(\tau)\}|_p = \frac{1}{p^2\pi^2}\frac{\sin(p\pi(1-d))}{d(1-d)}. \quad (17)$$

It is worth noting that the module of the first harmonic (i.e., $p = 1$) is more than double other high-order harmonics and its amplitude is quite flat as d varies. This permits us to consider that the carrier energy is almost entirely concentrated in this first harmonic, allowing us to approximate the HF current spectrum as (15) shifted around the carrier frequency f_m and scaled by (17) for $p = 1$. Since the codomain of the d-dependent term in (17) is $[\pi, 4]$, the worst case is considered (i.e., $d = 0.5$) to determine the estimated HF current ripple spectrum $\widetilde{i}_{g,\mathrm{HF}}$. Then,

the magnitude of nth spectral component of $\widetilde{i}_{g,\mathrm{HF}}$ is

$$\widetilde{\mathcal{I}}_{g,\mathrm{HF}}^n = \left|\mathcal{F}\left\{\widetilde{i}_{g,\mathrm{HF}}\right\}\right|_{f=f_m\pm nf_g} = \frac{V_N}{\pi^2 f_m L_g}\left|J_n(\pi U_g)\right| \quad (18)$$

which is the aimed at approximating the single-sideband harmonics around f_m in a closed form.

The spectrum description provided by (18) allows different simplified approaches in the design of ML converters as follows:

1) calculating the total rms current associated with the harmonics around the switching frequency f_m for the bandwidth required by EMI standards, Raggl et al. [11] and Liserre et al. [12] define a design procedure for the differential mode filter;

2) starting from (18) is possible to estimate the current spectrum through the common EMI receivers (e.g., peak, quasi-peak, or average) to evaluate the compliance with EMI standards [13];

3) the knowledge of the rms current for each HF harmonics allows the estimation of conduction losses in the grid-tied inductor calculating the ac resistance at each frequency.

The same approach can be used in the calculation of the magnetic core losses by applying Steinmetz's equation at each current harmonics for the major and minor B–H loop [14], [15].

III. EXPERIMENTAL VALIDATION

A single-phase ML converter is considered. The prototype is based on an Imperix B-Board PRO controller and several half-bridge modules. The main core of the converter is implemented by four series-connected full-bridges controlled with classical interleaved PWM modulation. Each module is supplied at $V_N = 25\,\mathrm{V}$ and switches at $10\,\mathrm{kHz}$. Different configurations of the ML converter have been considered, in terms of a number of voltage levels N_L and modulation index U_g. A subset of experimental configurations is reported in Table I, where the four highest harmonics of i_g around the effective switching frequency f_m are shown in descending order. The ith peak is located at $f = f_m \pm n_i f_g$ and is identified by the measured value $\mathcal{I}_i^\wedge$ and the estimated one $\widetilde{\mathcal{I}}_i^\wedge = \widetilde{\mathcal{I}}_{g,\mathrm{HF}}^{n_i}$ calculated from (18). To measure estimation effectiveness, the percentage of relative error $\Delta_i^\%$ is referred to herein

$$\Delta_i^\% = 100\frac{\widetilde{\mathcal{I}}_i^\wedge - \mathcal{I}_i^\wedge}{\mathcal{I}_1^\wedge} \quad (19)$$

where the difference between the magnitudes of estimated and the measured harmonics is normalized with the dominant component $\mathcal{I}_1^\wedge$. This allows us to weight the estimation error through the side-band harmonics, keeping the focus both on the shape of the estimated spectrum and on the maximum peak for EMI compliance. From the experimental measurements, it is notable that the maximum error for the highest peak $\mathcal{I}_1^\wedge$ is always less than 3% while for the other harmonics is limited to 10%. Fig. 6(a) and (c) displays the grid current spectrum around f_m of the configurations highlighted in Table I and shows that the peaks given by (18) well approximate the measured ones. Fig. 6(d) and (f) shows that the frequency dependence of the magnitude expressed in (17) by the term $p = f/f_m$ is well modeled and

TABLE I
MEASURED AND ESTIMATED HARMONICS OF HF GRID CURRENT COMPONENT FOR DIFFERENT ML-CONVERTER CONFIGURATIONS*

N_L	U_g	f_m	n_1	$\mathcal{I}_1^\wedge$	$\widetilde{\mathcal{I}}_1^\wedge$	$\Delta_1^\%$	n_2	$\mathcal{I}_2^\wedge$	$\widetilde{\mathcal{I}}_2^\wedge$	$\Delta_2^\%$	n_3	$\mathcal{I}_3^\wedge$	$\widetilde{\mathcal{I}}_3^\wedge$	$\Delta_3^\%$	n_4	$\mathcal{I}_4^\wedge$	$\widetilde{\mathcal{I}}_4^\wedge$	$\Delta_4^\%$
2	0.80	10	0	52.68	52.75	0.13	2	41.14	41.34	0.38	4	12.14	12.15	0.03	-	-	-	-
2	0.85	10	0	52.12	52.18	0.12	2	42.05	42.24	0.37	4	13.79	14.17	0.73	-	-	-	-
3	0.75	10	1	38.86	39.02	0.41	3	29.64	30.13	1.28	5	7.53	8.04	1.30	-	-	-	-
3	0.85	10	1	37.53	37.63	0.26	3	32.00	32.46	1.22	5	12.33	12.88	1.47	-	-	-	-
5	0.80	20	3	29.65	29.66	0.04	1	28.33	28.91	1.96	5	26.50	26.98	1.63	7	12.41	13.32	3.06
5	0.85	20	1	28.79	29.31	1.82	3	28.16	27.93	-0.77	5	27.72	28.17	1.55	7	15.51	16.02	1.77
7	0.75	40	5	25.63	25.67	0.15	7	22.04	22.64	2.34	3	19.32	20.25	3.66	9	10.30	10.94	2.48
7	0.85	40	7	24.63	25.14	2.10	3	23.73	24.29	2.27	1	21.62	22.47	3.45	5	21.07	20.27	-3.23
9	0.80	80	9	21.32	21.90	2.73	7	19.62	18.86	-3.57	5	19.44	20.09	3.02	11	14.09	14.58	2.33
9	0.85	80	9	22.13	22.41	1.28	5	20.28	20.76	2.16	3	17.20	18.18	4.42	11	16.90	17.40	2.25

*Switching frequency f_m expressed in kilohertz. Measured and estimated harmonic magnitudes $\mathcal{I}_i^\wedge$ and $\widetilde{\mathcal{I}}_i^\wedge$ expressed in $\mathrm{dB_{mA}}$. Other quantities are dimensionless. Shaded rows are test points reported in Fig. 6.
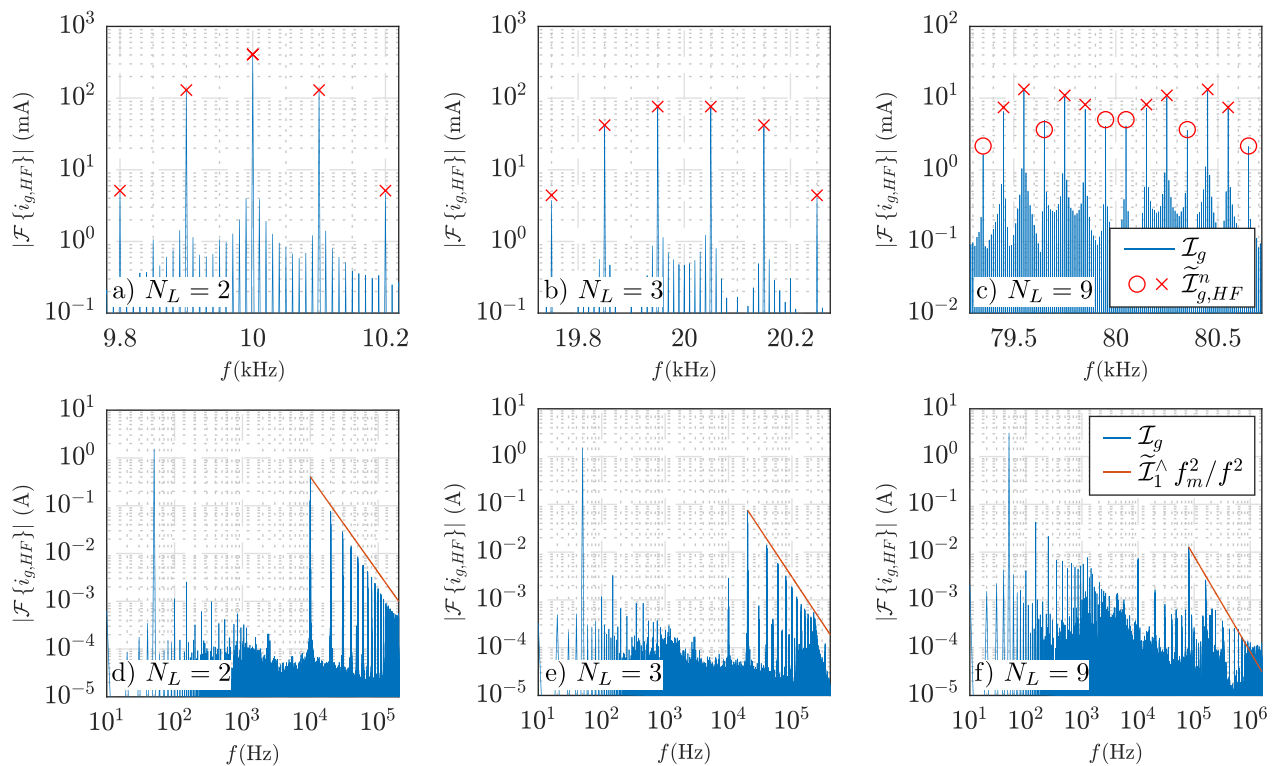

Fig. 6. Experimental results of current spectrum for different configurations of ML-converter prototype. (a) and (d) $N_L = 2$, $U_g = 0.85$. (b) and (e) $N_L = 3$, $U_g = 0.75$. (c) and (f) $N_L = 9$, $U_g = 0.85$. In (a)–(c), the peaks marked with $\times$ are also reported in Table I.

$\widetilde{\mathcal{I}}_1^\wedge f_m^2/f^2$ can be considered as an upper limit for $f < 20 f_m$. A further outcome of this approach is a rough estimation of HF rms current going through Parseval's theorem, which is useful for the evaluation of the winding and core losses in the inductor.

from the literature where the simulation approach is widely used, the model discussed herein allows us to a straightforward closed-form expression useful to perform analyses relevant to, for example, the IEEE 519-2014 standard compliance and the HF rms input current that impact the design of the EMI and input inductor filters.

IV. CONCLUSION

This letter proposes a simple yet accurate method to estimate the input current spectrum of the ML converter. The model is validated by means of simulations and experimental measurements on an ML prototype implemented. Differently

ACKNOWLEDGMENT

REFERENCES

[1] J. W. Kolar and T. Friedli, "The essence of three-phase PFC rectifier systems – Part I," *IEEE Trans. Power Electron.*, vol. 28, no. 1, pp. 176–198, Jan. 2013.

[2] T. Friedli, M. Hartmann, and J. W. Kolar, "The essence of three-phase PFC rectifier systems—Part II," *IEEE Trans. Power Electron.*, vol. 29, no. 2, pp. 543–560, Feb. 2014.

[3] S. Qin, Y. Lei, Z. Ye, D. Chou, and R. C. N. Pilawa-Podgurski, "A high-power-density power factor correction front end based on seven-level flying capacitor multilevel converter," *IEEE Trans. Emerg. Sel. Topics Power Electron.*, vol. 7, no. 3, pp. 1883–1898, Sep. 2019.

[4] Q. Huang, Q. Ma, P. Liu, A. Q. Huang, and M. A. de Rooij, "99% efficient 2.5-kW four-level flying capacitor multilevel GaN totem-pole PFC," *IEEE Trans. Emerg. Sel. Topics Power Electron.*, vol. 9, no. 5, pp. 5795–5806, Oct. 2021.

[5] J.-S. Kim, S.-H. Lee, W.-J. Cha, and B.-H. Kwon, "High-efficiency bridgeless three-level power factor correction rectifier," *IEEE Trans. Ind. Electron.*, vol. 64, no. 2, pp. 1130–1136, Feb. 2017.

[6] D. G. Holmes and T. A. Lipo, *Pulse Width Modulation for Power Converters: Principles and Practice*. Hoboken, NJ, USA: Wiley, 2003.

[7] Z. Wang et al., "A review of EMI research in modular multilevel converter for HVDC applications," *IEEE Trans. Power Electron.*, vol. 37, no. 12, pp. 14482–14498, Dec. 2022.

[8] Q. Tu and Z. Xu, "Impact of sampling frequency on harmonic distortion for modular multilevel converter," *IEEE Trans. Power Del.*, vol. 26, no. 1, pp. 298–306, Jan. 2011.

[9] R. Darus, G. Konstantinou, J. Pou, S. Ceballos, and V. G. Agelidis, "Carrier interleaved PWM techniques in modular multilevel converters: A comparison based on same voltage level waveforms," in *Proc. IEEE Energy Convers. Congr. Expo.*, 2014, pp. 3725–3730.

[10] M. Abramowitz and I. A. Stegun, *Handbook of Mathematical Functions With Formulas, Graphs, and Mathematical Tables*, M. D. of the National Research Council, Ed. Gaithersburg, MD, USA: Nat. Bureau Standards, 1972.

[11] K. Raggl, T. Nussbaumer, and J. W. Kolar, "Guideline for a simplified differential-mode EMI filter design," *IEEE Trans. Ind. Electron.*, vol. 57, no. 3, pp. 1031–1040, Mar. 2010.

[12] M. Liserre, F. Blaabjerg, and S. Hansen, "Design and control of an LCL-filter-based three-phase active rectifier," *IEEE Trans. Ind. Appl.*, vol. 41, no. 5, pp. 1281–1291, Sep./Oct. 2005.

[13] H. Li and K. Y. See, "Conversion factors between common detectors in EMI measurement for impulse and Gaussian noises," *IEEE Trans. Electromagn. Compat.*, vol. 55, no. 4, pp. 657–663, Aug. 2013.

[14] Y.-Y. Huang and Y.-S. Lai, "Novel efficiency optimized inductor design for GaN-based totem-pole PFC," in *Proc. IEEE 31st Int. Symp. Ind. Electron.*, 2022, pp. 933–938.

[15] A. De Bastiani Lange and M. L. Heldwein, "Optimal inductor design for single-phase three-level bridgeless PFC rectifiers," in *Proc. Braz. Power Electron. Conf.*, 2017, pp. 1–6.